

# Enhancing chaos in multistability regions of Duffing map for an image encryption algorithm

Hayder Natiq · Animesh Roy · Santo Banerjee · Amar P. Misra · N. A. A. Fataf

the date of receipt and acceptance should be inserted later

**Abstract** This paper investigates and analyzes the dynamics of the two-dimensional Duffing map. Multistability behavior has been observed from the system numerically. Such behavior, especially the coexistence of chaotic and periodic attractors, is undesirable in the applications of chaos-based cryptography. Therefore, we design and implement a Sine-Cosine chaotification technique to enhance chaos in the multistable regions. Furthermore, this paper proposes a new image encryption algorithm to examine the performance of the generalized Duffing map in cryptography applications. Simulation results and security analysis reveal that the proposed algorithm can effectively encrypt and decrypt several image types with a high level of security.

**Keywords** 2D Duffing map · Coexisting attractors · Hyperchaotic behavior · Image encryption

Hayder Natiq  
Information Technology Collage, Imam Ja'afar Al-Sadiq University, Iraq

Animesh Roy  
Department of Mathematics, Siksha Bhavana, Visva-Bharati University, Santiniketan, 731 235, India

Santo Banerjee  
Department of Mathematical Sciences, Giuseppe Luigi Lagrange, Politecnico di Torino, Corso Duca degli Abruzzi 24, Torino, Italy  
E-mail: santoban@gmail.com

Amar P. Misra  
Department of Mathematics, Siksha Bhavana, Visva-Bharati University, Santiniketan, 731 235, India

N. A. A. Fataf  
Centre for Defence Foundation Studies, Universiti Pertahanan Nasional Malaysia, Sungai Besi, Malaysia

## 1 Introduction

Information security has become crucial due to the rapid development of multimedia and Internet technology, especially images, that are shared online. Recent security analyses revealed that the classic encryption algorithms, such as Advanced Encryption Standard (AES) and Data Encryption Standard (DES), are undesirable for images because of their characteristics [1]. Therefore, several approaches for increasing security have been proposed, such as cellular automata [2], DNA coding [3], compressive sensing [4, 5], wavelet transmission [6], and chaos [7, 8]. Due to the high security and fast speed of the chaos-based image encryption technique and the similarity between the features of chaotic systems and images, this technique has become widely used and most preferable in cryptography applications [9, 10, 11].

Many image encryption schemes have thus been developed using chaotic systems [12, 13, 14, 15, 17, 18, 19, 20]. It has been established that the security level of a chaos-based encryption algorithm is highly dependent on the characteristics of the employed chaotic maps [21]. However, recent investigations have revealed that numerous employed maps can have some drawbacks, such as chaos degradation with finite precision platforms, low complex performance, narrow and discontinuous chaotic ranges [22]. In this way, several studies have been performed to improve the characteristic of chaotic maps by proposing different chaotification techniques. For example, Hua et al. [25, 23] enhanced the chaotic behaviors of the Logistic map by modulating its output using a nonlinear transform. Natiq et al. [24] enhanced the chaos complexity of the 2D Henon map using a Sine map for image encryptions. Hua et

al. [26] proposed a Cosine chaoticification technique to generate robust chaotic maps for encrypting images.

However, some investigations on the dynamics of chaotic systems have discovered appealing nonlinear phenomena, namely multistability behaviors or coexisting attractors [27]. Multi-stable chaotic systems can exhibit more than one chaotic or periodic attractor with appropriate initial conditions. Multi-stable chaotic systems with continuous-time have been presented during the last few years [28]. Meanwhile, little attention has been focused on the multistability in discrete-time chaotic systems or maps [29]. Note that a multi-stable system with coexisting chaotic and periodic attractors is not preferable in cryptography applications. Therefore, it is crucial to determine either the regions of coexisting only chaotic attractors or a suitable chaoticification technique to enhance chaos in the multistability regions.

In this work, we revisit the dynamics of a 2D discrete chaotic system, namely, the 2D-Duffing map. The numerical investigations show that the Duffing map can produce multistability behaviors in which the coexistence of chaotic and non-chaotic attractors and the coexistence of two chaotic attractors can observe with a specific set of system parameters. It is imperative to note that such complicated behavior is rare in low-dimensional chaotic maps. Therefore, we introduce a chaoticification technique based on two trigonometric functions to overcome this situation. Dynamical properties show that the proposed chaoticification technique can improve the chaotic and non-chaotic attractors to become hyperchaotic attractors. Besides, it enhances the unpredictability and randomness of the map. Based on the generalized Duffing map, we propose a new image encryption algorithm with the principles of confusion and diffusion. Firstly, the hyperchaotic sequences are generated for scrambling of plain-image pixels. Then, the diffusion process is accomplished by the elliptic curves, S-box, and hyperchaotic sequences. The simulation results confirm that the proposed encryption algorithm can effectively encrypt various kinds of digital images including Grey-scale, RGB, medical, and hand writing images. Security analysis shows that this algorithm can resist common attacks, such as statistical, differential, known plaintext attack and chosen plaintext attack. Efficient analysis indicates that it has low computation and time complexity. Therefore, it has excellent application prospect.

This paper is arranged as follows: Section 2 describes the dynamics of the 2D-Duffing map. In Section 3, we introduce a chaoticification approach to enhance chaos complexity of the 2D-Duffing map, and then calculate the performance of the enhance map. Section 4 introduces an image encryption algorithm

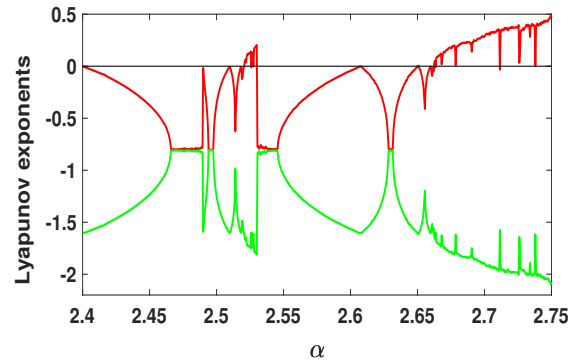


Fig. 1: Lyapunov exponents of the Duffing map (1) with the parameter  $\beta = 0.2$  and the initial condition  $(0.25, 0.77)$ .

based on the enhanced Duffing map. Simulation results for image encryption using some existing schemes and our proposed scheme are presented in Section 5. Section 6 is left to perform the security analysis of encrypted images. Finally, Section 7 concludes the results.

## 2 The Duffing model

The Duffing map, also known as the Holmes map [30], is a 2D discrete-time chaotic system, given by,

$$\begin{cases} x_1(n+1) = x_2(n), \\ x_2(n+1) = -\beta x_1(n) + \alpha x_2(n) - x_2^3(n), \end{cases} \quad (1)$$

where the parameters  $\alpha$  and  $\beta$  are positive.

### 2.1 Stability of equilibrium points

From a graphical point of view, a point  $E$  is said to be an equilibrium point of the function  $G(x)$  only if  $G^n(E) = E$ . Thus, one can obtain the equilibrium points of the system (1) by reducing its dimension as follows:

$$x_1^{(v)} = -\beta x_1^{(v)} + \alpha x_1^{(v)} - (x_1^{(v)})^3, \quad (2)$$

where  $v = 1, 2, \dots$ . For the parameters  $\alpha = 2.75$  and  $\beta = 0.2$ , the equilibrium points can be obtained as:

$$\begin{cases} E_1 = (0, 0), \\ E_2 = (1.244, 1.244), \\ E_3 = (-1.244, -1.244). \end{cases}$$

The stability of the equilibrium points is determined by the following Jacobian matrix of the Duffing map (1).

$$J = \begin{pmatrix} \frac{\partial f_1}{\partial x_1} & \frac{\partial f_1}{\partial x_2} \\ \frac{\partial f_2}{\partial x_1} & \frac{\partial f_2}{\partial x_2} \end{pmatrix}.$$

Next, the Duffing map (1) can be linearized with respect to an equilibrium point  $E_i = (x_1^*, x_2^*)$  by

$$J_{E_i} = \begin{pmatrix} 0 & 1 \\ -\beta & \alpha - 3(x_2^*)^2 \end{pmatrix}.$$

The corresponding eigenvalues at  $E_i$  can be obtained by solving  $\det(\lambda I - J_{E_i}) = 0$ , which yields

$$\lambda^2 + (3(x_2^*)^2 - \alpha)\lambda + \beta = 0.$$

Thus, the eigenvalues are given by

$$\begin{cases} \lambda_1 = \frac{3(x_2^*)^2 - \alpha - \sqrt{(3(x_2^*)^2 - \alpha)^2 - 4\beta}}{2} \\ \lambda_2 = \frac{-3(x_2^*)^2 + \alpha + \sqrt{(3(x_2^*)^2 - \alpha)^2 - 4\beta}}{2} \end{cases}.$$

In discrete dynamical systems, the stability of equilibrium points is dependent on the corresponding eigenvalues. If an eigenvalue lies the interval  $[-1, 1]$ , then the equilibrium point is said to exhibit a stable state. Otherwise, it represents an unstable state. For the parameters  $\alpha = 2.75$  and  $\beta = 0.2$ , the stability of the equilibrium points of the Duffing map (1) is illustrated in Table 1. Clearly, the Duffing map has one unstable and two stable equilibrium points.

Table 1: The equilibria of Duffing map (1) and their stability for the parameters  $\beta = 0.2$  and  $\alpha = 2.75$ .

Equilibria	$\lambda_1$	$\lambda_2$	Stability analysis
$E_1$	-2.6752	2.6752	unstable equilibrium
$E_2$	0.1123	-0.1123	stable equilibrium
$E_3$	0.1123	-0.1123	stable equilibrium

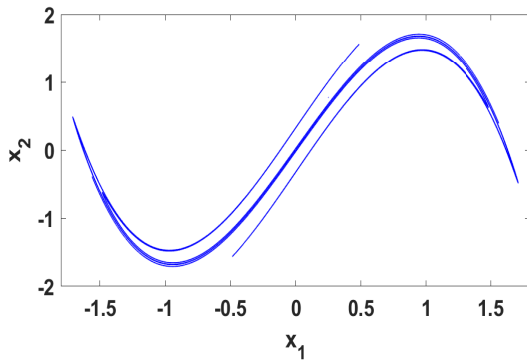


Fig. 2: Chaotic attractor of the Duffing map (1) with the parameter  $\beta = 0.2$ ,  $\alpha = 2.75$  and for the initial conditions  $(0.25, 0.77)$ .

## 2.2 Self-excited chaotic attractor

To investigate the dynamical behaviors of the map (1), we calculate the Lyapunov exponents (LE) as depicted in Figure 1 corresponding to the initial conditions  $(0.25, 0.77)$ . It is seen that the map (1) exhibits two different behaviors in one of which it exhibits chaos where the largest Lyapunov exponent (LLE) is positive, and in the other it shows periodic behaviors with LLE is zero or negative. Figure 2 demonstrates the chaotic behaviors of the Duffing map corresponding to the parameters  $\alpha = 2.75$  and  $\beta = 0.2$ . Furthermore, since the map (1) has one unstable equilibrium point corresponding to a different set of parameters  $\alpha = 2.75$  and  $\beta = 0.2$ , the chaotic attractor in Figure 2 is self-excited [27].

## 2.3 Coexisting attractors

Multistability behaviors or coexisting attractors indicate that the nonlinear dynamical system can produce two or more attractors by changing the initial conditions. The coexistence of attractors is a phenomenon that happens in nonlinear dynamical systems due to

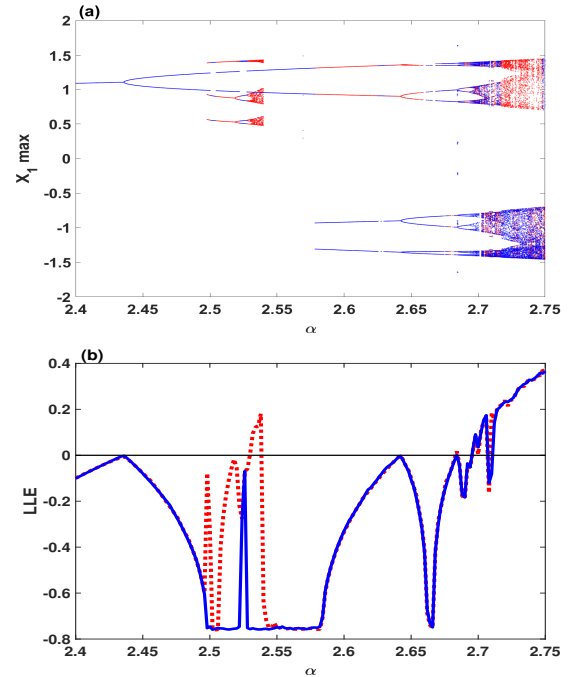


Fig. 3: Coexisting two attractors with the parameter  $\beta = 0.218$ , and under two sets of initial states in which the blue and red orbits are initiated from  $(0.25, 0.97)$  and  $(0.25, 0.77)$  respectively: (a) Bifurcation diagram with respect to the variable  $x_1$ ; (b) Largest Lyapunov exponents.

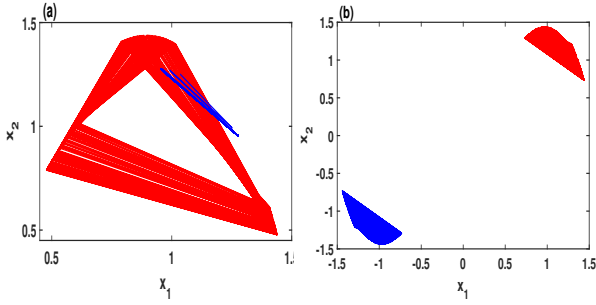


Fig. 4: Multistability behaviors of the Duffing map (1) under different initial conditions (0.25, 0.77) (red) and (0.25, 0.97) (blue): (a) the coexistence of chaotic and periodic orbit with the parameters  $\alpha = 2.5392$ , and  $\beta = 0.218$ ; (b) the coexistence of two chaotic attractors with the parameters  $\alpha = 2.73$ , and  $\beta = 0.218$ .

the high sensitivity of such systems to their initial conditions. In this subsection, we demonstrate the existing of multistability behaviors in the Duffing map (1) by considering an appropriate set of initial conditions. Such complicated behaviors of the Duffing map have not been studied in the previous studies.

For a fixed value of  $\beta$ , i.e.,  $\beta = 0.218$ , when the parameter  $\alpha$  is varied from 2.4 to 2.75, the coexisting bifurcation model and the LE of the Duffing map (1) corresponding to the initial conditions (0.25, 0.97) (blue), (0.25, 0.77) (red) are plotted as shown in Figure 3. It is seen that the coexistence of self-excited chaotic attractors and the periodic orbits occur mainly in the region  $2.532 \leq \alpha \leq 2.539$ . However, two self-excited chaotic attractors can also coexist in some other region of  $2.71 \leq \alpha \leq 2.74$ . To further visualize these interesting features, we consider two other values of  $\alpha$ , i.e.,  $\alpha = 2.5392$  and 2.73. The results are displayed in Figure 4 (a) and (b) respectively. As can be seen in Fig. 4 (a), the Duffing map (1) shows the coexistence of a chaotic attractor and periodic orbit. Furthermore, this map shows in Fig. 4 (b) the coexistence of two chaotic attractors located in different positions depending on the location of the two unstable equilibria  $E_2$  and  $E_3$ .

It is to be noted that the keys in the chaos-based cryptosystems are typically formed by means of the initial conditions and the parameters of the chaotic map. However, when the chaotic map exhibits multistability behaviors, such as the coexistence of chaotic attractors and periodic orbits, the corresponding cryptosystems will be insecure. In this situation, one requires to introduce an efficient chaotification technique on 2D Duffing map (1) for enhancing chaos in the non-chaotic regions.

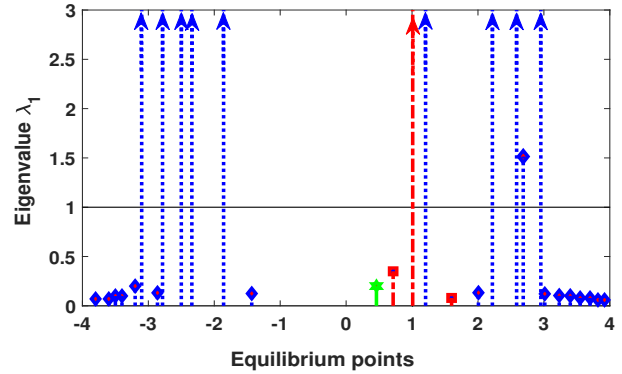


Fig. 5: Equilibrium points of the enhanced Duffing map (3) and its stability when the parameters  $\alpha = 2.75$  and  $\beta = 0.2$ : 1) for  $A = 1$  and  $B = 1$ , there is only one stable equilibrium point (green color); 2) for  $A = 2$  and  $B = 3$ , there are three equilibria (red color) in which two stable and one unstable; 3) for  $A = 15$  and  $B = 3.7$ , there are 25 equilibria (blue color) in which 15 stable and 10 unstable.

### 3 Sine-Cosine chaotification technique

This section proposes a new chaotification technique that uses two trigonometric functions as nonlinear transforms to the outputs of the Duffing map (1). The Sine and Cosine functions are applied to enhance the chaos and complexity of the Duffing map in the chaotic region. Moreover, these functions can also be used to produce chaos in the non-chaotic regions.

The structure of the proposed technique is shown in Figure 6, where  $f(y(n))$  and  $g(x(n), y(n))$  are two seed maps taken from Eq. (1). Mathematically, the proposed map can be defined as follows

$$\begin{cases} x(n+1) = A \sin(y(n)), \\ y(n+1) = B \cos(-\beta x(n) + \alpha y(n) - y^3(n)), \end{cases} \quad (3)$$

where  $A (> 0)$ , and  $B (> 0)$  are parameters.

#### 3.1 Stability analysis of the enhanced Duffing map

In the previous section 2.1, we have seen that the Duffing map (1) has three equilibrium points in which two of them are stable and the other unstable, as illustrated in Table 1. So, it is interesting to know whether the enhanced Duffing map (3) generates the same numbers or different numbers of equilibria when  $\alpha = 2.75$  and  $\beta = 0.2$ . Besides, it is important to investigate the stability of these equilibria.

We note that the eigenvalues of the enhanced Duffing map satisfy the relation  $\lambda_1 = -\lambda_2$ . Three cases may be of interest to investigate the stability of equilibrium

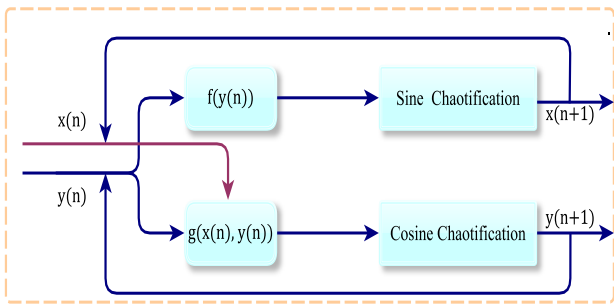


Fig. 6: Structure of the enhanced Duffing map.

points of the enhanced Duffing map: 1) when  $A = 1$  and  $B = 1$ , the enhanced Duffing map (3) has only one stable equilibrium point, as shown in the green color of Figure 5; 2) when  $A = 2$  and  $B = 3$ , the enhanced Duffing map (3) has three different equilibria in which two of them are stable and one unstable, as shown in the red color of Figure 5. 3) when  $A = 15$  and  $B = 3.7$ , the enhanced Duffing map (3) has 25 different equilibria in which 15 equilibria are stable and 10 equilibria are unstable, as shown in the blue color of Figure 5.

Thus, it can be concluded that depending on the values of the parameters  $A$  and  $B$ , the enhanced Duffing map (3) can generate equilibrium points less than or equal to or greater than those of the Duffing map (1).

### 3.2 Enhancing chaos of Duffing map

Since the number of equilibria of the enhanced map (3) can be larger than those of the original map when the parameters  $A$  and  $B$  are large enough [See the third case in Figure 5], it is quite reasonable to assume that increasing the equilibria of a dynamical system in a limited range can enhance chaos with overlapping co-existing attractors.

In order to graphically demonstrate the above features, we consider the parameters of the enhanced map (3) as  $\beta = 0.218$ ,  $A = B = 4.5$  for which the map has 37 equilibrium points distributed within the range  $[-3.89, 3.97]$ . Figure 7 (a) and (b) depict the coexisting bifurcation model and LLE of the Duffing map (1) corresponding to two sets of initial conditions (0.25, 97) (blue), (0.25, 0.77) (red). Clearly, the chaotic regions of the 2D Duffing map are enhanced and the non-chaotic regions shift to the chaotic regions. Furthermore, the two coexisting chaotic attractors of the enhanced map (3) are overlapped, and occupied a much larger region in the 2D phase space, as can be seen in Figure 7 (c).

### 3.3 Generating hyperchaotic behaviors

A nonlinear dynamical system exhibits hyperchaotic behaviors only when it has at least two positive values of the LEs. So, the 2D Duffing map (1) exhibits no hyperchaotic behavior as it has only one positive value of the LE with some parameter values (See Figure 1). Typically, the trajectory of a dynamical system with hyperchaotic behavior is more difficult to predict than chaotic ones, and so is desirable for cryptography applications.

To examine the occurrence of hyperchaotic behaviors in the enhanced Duffing map (3), we calculate the LEs when both the parameters  $A$  and  $B$  vary as shown in Figure 8. The LLE of the enhanced map (3) is illustrated in Figure 8 (a), while the lowest LE is illustrated in Figure 8 (b). It is seen that the enhanced map shows chaotic behaviors with higher values of the LLE when  $B \in (7.3, 15]$  and for any value of the parameter  $A$ . However, the hyperchaotic behaviors of the enhanced map are observed in two regions as follows: 1)  $A \in [12, 15]$  and  $B \in [4, 7.3]$ ; 2)  $A \in [3, 15]$  and  $B \in [2, 4]$ .

In order to verify the features of the enhanced Duffing map (3) that the hyperchaotic attractor has high level of complexity and spreads in a wide region of the 2D phase space, we plot the hyperchaotic attractor of the enhanced map as well as the attractors of other chaotic and hyperchaotic maps as shown in Figure 9. Here, the 2D-SLMM [25], 2D-SIMM [31], 2D-LASM [23], and 2D-LICM [17] are considered as hyperchaotic maps, while the 2D Ushiki [32] as a chaotic map.

Figure 9 shows that the attractor of the enhanced map with the parameters  $\alpha = 1$ ,  $\beta = 5$ ,  $A = 15$ ,  $B = 3.7$  occupies the whole 2D phase space with regions  $x \in [-15, 15]$  and  $y \in [-3.7, 3.7]$ . This means that the enhanced map generates some extreme unpredictable sequences, and its ergodicity property is much better than other maps.

### 3.4 Complexity based Sample Entropy

Richman et al. [33] introduced an approach to develop an Approximate Entropy, which is widely used as a measure for estimating the time series complexity. Several analyses have demonstrated that the developed measure, namely, the Sample Entropy (SamEn) is more accurate than Approximate Entropy.

To illustrate the complexity of the enhanced map (3), Figure 10 depicts the SamEn results of the enhanced map and different chaotic and hyperchaotic maps. The parameters of the enhanced map (3) for this figure are considered as  $\beta = 5$ ,  $A = 15$ , and  $B = 3.7$ . Clearly, the

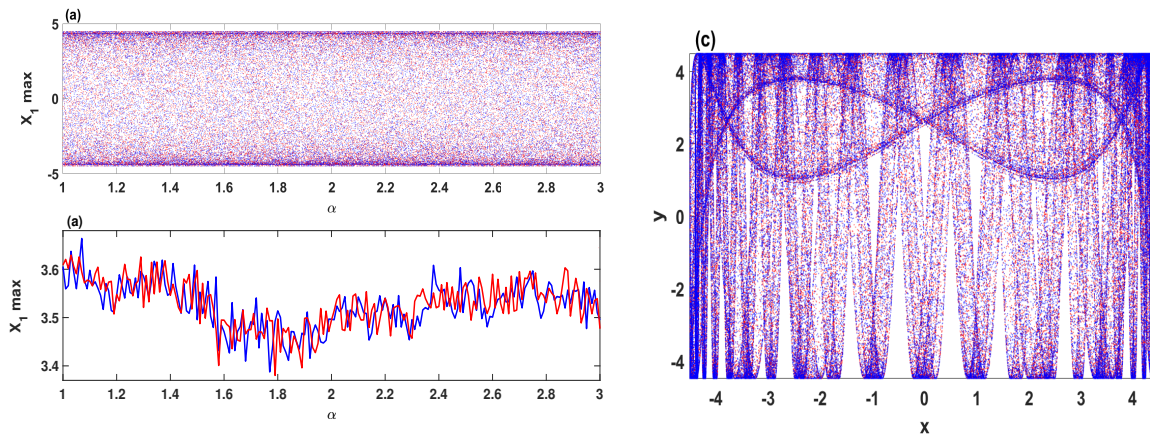


Fig. 7: Dynamics of the enhanced Duffing map (3) under the initial conditions  $(0.25, 0.77)$  (red) and  $(0.25, 0.97)$  (blue) with the parameters  $\beta = 0.218$ ,  $A = B = 4.5$ : (a) the coexisting bifurcation model; (b) Largest Lyapunov exponents; (c) phase space with  $\alpha = 1$ .

enhanced map (3) has the largest SamEn values implying that one needs more information to predict the generated sequences by this map.

### 3.5 Randomness analysis

The randomness of two hyperchaotic sequences  $\{x\}$  and  $\{y\}$ , so generated by the enhanced Duffing map (3), can be examined by several randomness evaluation meth-

ods. Here, we use the software package of FIPS 140-2, which mainly consists of three different tests. For each test, the p- value is derived to reflect the randomness level. A chaotic sequence can pass the test when the derived p-value is within a range of  $[10^{-4}, 1 - 10^{-4}]$ . The experimental results are shown in Table 2. As can be seen that the sequences  $\{x\}$  and  $\{y\}$  pass all the statistical tests, which means that these two sequences are reliable PRNG, and have excellent randomness property.

In summary, Lyapunov exponents, trajectory, SamEn, and FIPS 140-2 have demonstrated that the enhanced map (3) exhibits decent ergodicity property, wide hyperchaotic behavior, high level of complexity and randomness. As a result, the enhanced map would be very promising for cryptography applications.

## 4 Chaos based image encryption and decryption

This section introduces a new image encryption algorithm. Figure 12 illustrates the structure of the proposed algorithm, which achieves the confusion and diffusion processes by the hyperchaotic sequences and elliptic curve over the Galois field  $GF_{2^8}$ . Specifically, the enhanced Duffing map (3) is used to generate hyperchaotic sequences for scrambling the pixels of a plain-image through image scrambling algorithm. Subsequently, the diffusion process is accomplished by field matrix, S-box, and hyperchaotic sequence. Simulations results demonstrate that the proposed encryption algorithm gives the users a flexibility to encrypt several kinds of images such as Grey scale, Medical, and RGB images with a higher level of security.

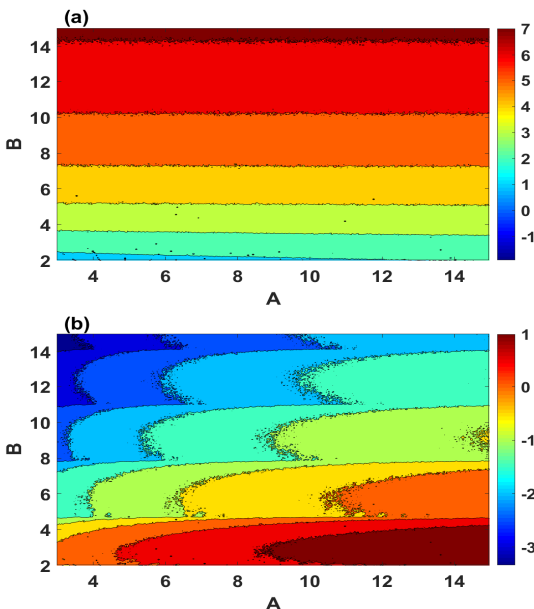


Fig. 8: Hyperchaotic diagram of the enhanced Duffing map (3) based on Lyapunov exponents with  $\beta = 5$ ,  $\alpha = 1$ : (a) the largest Lyapunov exponent; (b) the lowest Lyapunov exponent.

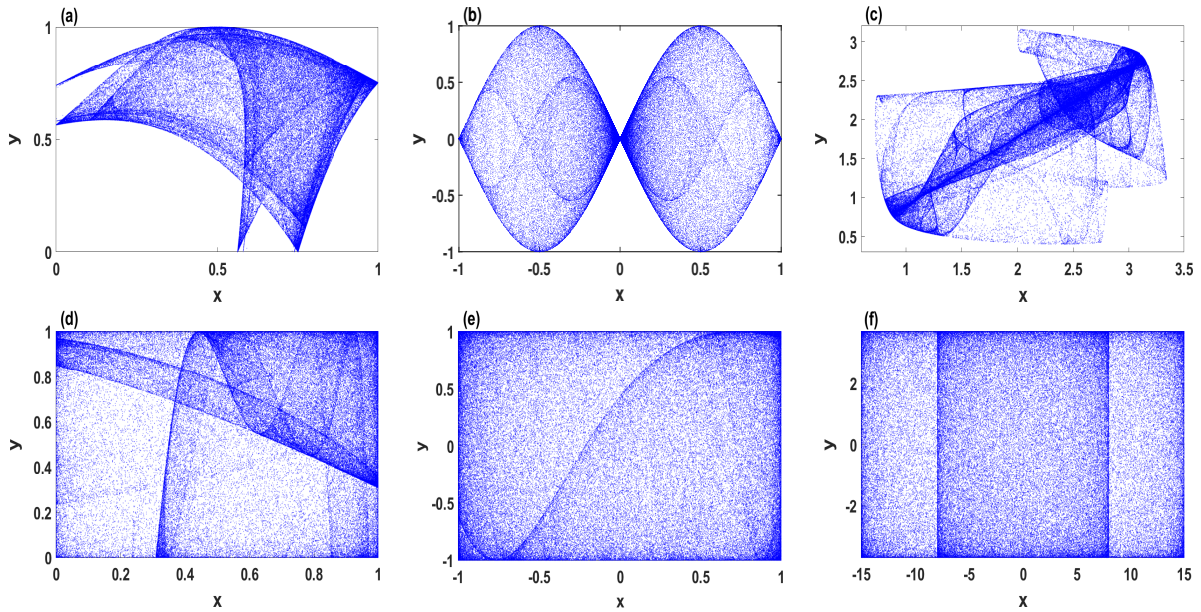


Fig. 9: Chaotic and hyperchaotic attractors of different 2D maps: (a) 2D-SLMM [25]; (b) 2D-SIMM [31]; (c) 2D Ushiki map [32]; (d) 2D-LASM [23]; (e) 2D-LICM [17]; (f) the enhanced Duffing map (3).

Table 2: Randomness analysis test with FIPS-140-2 results of sequences  $x$  and  $y$  generated by the map 3.

Tests	Sub-tests	$x$	$y$	Decision
Runs test	P-value	0.3489	0.1546	Pass
	0 runs, length 1	2499	2413	Pass
	0 runs, length 2	1235	1186	Pass
	0 runs, length 3	612	604	Pass
	0 runs, length 4	305	312	Pass
	0 runs, length 5	152	157	Pass
	0 runs, length 6+	153	154	Pass
	Longest run of 0	14	14	Pass
	1 runs, length 1	2592	2489	Pass
	1 runs, length 2	1287	1257	Pass
	1 runs, length 3	646	645	Pass
	1 runs, length 4	320	334	Pass
	1 runs, length 5	166	170	Pass
	1 runs, length 6+	166	172	Pass
	Longest run of 1	14	13	Pass
Monobit test	P-value	0.3104	0.5489	Pass
	No. of 1s 20000-bitstream	10113	10039	Pass
Poker test	p-value	0.1440	0.1926	Pass
	Y- value	13.1008	17.5232	Pass

#### 4.1 Confusion based bit-plane transformation

An efficient encryption algorithm should disassemble the high correlations between adjacent pixels. These high correlations can be de-correlated by scrambling adjacent pixels to different positions. To ensure an efficient scrambling process, we divided the plain-images into 8-bit-plane. Then the positions of all adjacent pixels are randomly scrambled by the image scrambling

algorithm. The latter is demonstrated in Algorithm 1. The algorithm typically illustrates the pseudo-code of scrambling and de-scrambling processes.

#### 4.2 S-box and the field matrix

We construct the S-box and the field matrix based on the points of an elliptic curve over the Galois field  $GF_{2^n}$ . The description of the elliptic curve and its points is

given below. The elliptic curve is a set of points that satisfy the following Weierstrass equation:

$$E : y^2 + a_1xy + a_3y = x^3 + a_2x^2 + a_4x + a_6, \quad (4)$$

where  $a_1, a_2, a_3, a_4, a_5$ , and  $a_6$  represent the parameters and the initial conditions of the map (3)  $A, \alpha, B, \beta, IC_1$ , and  $IC_2$ , respectively.

The elliptic curve equation over the field  $GF_{2^8}$  is defined as

$$E_{2^8}(a, b) : y^2 + xy = x^3 + ax + b, \quad (5)$$

which is obtained by the following transformation

$$(x, y) \rightarrow \left( a_1^2x + \frac{a_3}{a_1}, a_1^3y + \frac{a_1^2a_4 + a_3^2}{a_1^3} \right),$$

where  $a_1 \neq 0$  and  $a, b \in F_{2^8}$ . Thus, the curve is defined over the field  $GF_{2^8}$ , and  $a$  and  $b$  are calculated as

$$a = \text{floor}(\text{mod}((a_3/a_1^3) + a_2/a_1^2) \times 10^5, 256), \quad (6)$$

$$b = \text{floor}(\text{mod}((c_2^2 + c_1^3 + c_1^2 + c_1 + a_6 + a_4 \cdot c_1) \times 10^5, 256))$$

with  $c_1 = a_3/a_1^3$  and  $c_2 = (a_3^2 \cdot a_4 + a_3^3)/a_1^6$ .

To construct the field matrix  $F$ , we first extract some points which satisfy Eq. (5), by means of the following primitive polynomial.

$$f(x) = 1 + x^2 + x^3 + x^4 + x^8.$$

Here, if the generator  $g$  satisfies  $f(g) = 0$ , one obtains  $g^8 = g^4 + g^3 + g^2 + 1$ , where  $g \equiv (00000010)$ . Thus, the properties of the points on elliptic curve  $E_{2^8}(a, b)$  over the field  $F_{2^8}$  can be stated as follows:

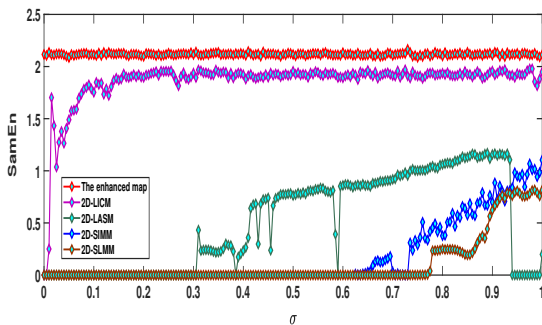


Fig. 10: SamEn results of different chaotic and hyperchaotic maps, where parameter  $\sigma$  represents  $\alpha, a, a_1, a_2, \alpha_1$ , for the enhanced map (3), 2D-LICM [17], 2D-LASM [23], 2D-SIMM [31], and 2D-SLMM [25], respectively.

---

### Algorithm 1: Image scrambling at bit level

---

**Input:** Plain-image of the size  $m \times n$ .

**Output:** The scrambled and de-scrambled images

- 1 Generate hyperchaotic sequences  $\{x\}$  and  $\{y\}$  with the long of  $k$ , where  $k \geq m \times n$ ;
  - 2 Calculate  $Sx = \text{ceil}(\text{mod}(x \times 10^5, 256))$  and to form matrix is of  $Sx_{m \times n} \leftarrow \text{Reshape}(Sx, m, n)$
  - 3 Calculate  $Sy = \text{ceil}(\text{mod}(y \times 10^4, m \times n))$  and to form a sequence where each element don't repeat and non zero
  - 4 % Image scrambling
  - 5 Reshape  $A_{m \times n} \leftarrow \{a(i)\}$  for  $i = 1, 2, \dots, m \times n$  and iterate  $a(Sy(i))$
  - 6 Reshape  $a(Sy(i)) \rightarrow A_{m \times n}$
  - 7 % Image de-scrambling
  - 8 Calculate  $\text{inv.}(Sy)$  from  $Sy$
  - 9 Reshape  $CI_{m \times n} \leftarrow \{a(i)\}$  for  $i = 1, 2, \dots, m \times n$  and iterate  $a(\text{inv.}(Sy(i)))$
  - 10 Reshape  $a(\text{inv.}(Sy(i))) \rightarrow \text{Decryptedimage}_{m \times n}$
  - 11 Divide the plain-image into 8-bit plane using i.e.  $A_{m \times n}(\text{plain-image}) = A_{m \times n \times 8}$
  - 12 Divide  $Sx$  into  $Sx_{m \times n \times 8}$
  - 13 Initialize A matrix  $B$  is of order  $m \times n \times 8$  i.e.  $B_{m \times n \times 8} = \text{zeros}(m, n, 8)$
  - 14 **for**  $k=1$  to 8 **do**
  - 15     **for**  $j=1$  to  $n$  **do**
  - 16         **for**  $i=1$  to  $m$  **do**
  - 17              $B(i, j, k) = \text{bitxor}(A(i, j, k), Sx(i, j, k))$
  - 18         **end**
  - 19     **end**
  - 20 **end**
  - 21 **Return**  $B$
  - 22 Set the bit position at each plain using the previous plane
  - 23 Initialize a scramble matrix  $Sc^0 = \text{zeros}(m, n)$
  - 24 **for**  $k=1$  to 8 **do**
  - 25      $Sc^k = \text{bitset}(B(:, :, k), Sc^{k-1})$
  - 26 **end**
  - 27 **Return**  $Sc_{m \times n}$
- 

- For any point  $P(x_p, y_p) \in E_{2^8}(a, b)$  satisfying Eq. (5) and if  $O$  is the additive identity, i.e.,  $P + O = P$  then  $-P = (x_p, x_p + y_p)$  and  $P - P = O$ .
- If  $P = (x_p, y_p)$ ,  $Q = (x_q, y_q) \in E_{2^8}(a, b)$  and  $P \neq \pm Q$ , then  $R = P + Q = (x_r, y_r)$ , where  $(x_r, y_r) = (\alpha^2 + \alpha + x_p + x_q + A, \alpha(x_p + x_r) + x_r + y_p)$  and  $\alpha = (y_q + y_p)/(x_p + x_q)$ . Again, if  $P = Q$ , then  $2P = (x_r, y_r) = (\lambda^2 + \lambda + A, x_p^2 + (\lambda + 1)x_r)$ , where  $\lambda = x_p + \frac{y_p}{x_p}$ .

The algorithm for the field matrix and its inverse is stated in Algorithm 2. The field matrix is constructed by the initial conditions  $IC_1$ , and  $IC_2$  of the enhanced map (3) and the primitive polynomial  $f(x)$ . It is imperative to note here that the field matrix is invertible over  $Z_2$ , which gives the possibility to generate the inverse S-Box for decryption process.

Next, in order to extract points  $P(x, y)$  to form the S-box of order  $16 \times 16$ , we require 256 number of points, i.e.  $P = [P_1, P_2, \dots, P_{256}]$  that satisfy Eq. (5). As an

**Algorithm 2:** The field matrix and its inverse.

---

**Input:** The initial conditions  $IC_1$ , and  $IC_2$ , as well as the primitive polynomial  $f(x)$ .

**Output:** The field matrix and inverse field matrix.

- 1 Calculate  $F(1) = \text{mod}(\text{dec2bin}(IC_1 \times IC_2 \times 10^3), f(x))$ ;
- 2 **while**  $i = 1, i++$  **do**
- 3      $F(i+1) = \text{mod}(\text{dec2bin}(F(i) \times IC_1 \times IC_2 \times 10^3), f(x))$   
       Calculate  $F = [F(1), F(2), \dots, F(8)]$
- 4     **if**  $\det(F) \neq 0$  over  $Z_2$  **then**
- 5         **return**  $F$
- 6     **else**
- 7         Calculate  $F = [F(i+1), F(i+2), \dots, F(i+8)]$
- 8     **end**
- 9 **end**
- 10 Get  $F_{8-bit \times 8-bit}$
- 11 To calculate inverse field matrix
- 12 Calculate  $F(1) = \text{mod}(\text{dec2bin}(IC_1 \times IC_2 \times 10^3), f(x))$
- 13 **while**  $i = 1, i++$  **do**
- 14      $\text{inv}.F(i+1) = \text{mod}(\text{dec2bin}(\text{inv}.F(i) \times IC_1 \times IC_2 \times 10^3), f(x))$   
       Calculate  $\text{inv}.F = [\text{inv}.F(1), \dots, \text{inv}.F(8)]$
- 15     **if**  $\det(F \times \text{inv}.F) = 1$  over  $Z_2$  **then**
- 16         **return**  $\text{inv}.F$
- 17     **else**
- 18         Calculate  $\text{inv}.F = [\text{inv}.F(i+1), \dots, \text{inv}.F(i+8)]$
- 19     **end**
- 20 **end**
- 21 Get  $\text{inv}.F_{8-bit \times 8-bit}$

---

**Algorithm 3:** The S-Box and its inverse.

---

**Input:** The sequences  $\{x_1\}$  and  $\{y_1\}$ , as well as the extract points  $P$ , field matrix  $F$  and  $f(x)$ .

**Output:** The S-Box and inverse S-Box.

- 1 Calculate  $\text{Index}_{256 \times 256}^1 \leftarrow \text{reshape}(x_1, 256, 256)$ ;
- 2 Calculate  $\text{Index}_{256 \times 256}^2 \leftarrow \text{reshape}(y_1, 256, 256)$ ;
- 3 **for**  $j=1$  to 256 **do**
- 4     **for**  $i=1$  to 256 **do**
- 5          $Sb(i) \leftarrow \text{Bin2Dec}(\text{mod}(\text{Dec2Bin}(\text{Index}^1(P(i, 1)) \otimes \text{Dec2Bin}(P(1, j))), f(x)))$ ;
- 6     **end**
- 7 **end**
- 8 Calculate  $SB_{16 \times 16} \leftarrow \text{reshape}(SB, 16, 16)$ ;
- 9 **for**  $j=1$  to 16 **do**
- 10     **for**  $i=1$  to 16 **do**
- 11          $S\text{-Box}(i, j) = \text{Bin2Dec}(\text{mod}([F]_{8 \times 8} \times [\text{Dec2Bin}(SB(i, j))]_{8 \times 1}, 2) \oplus \text{Dec2Bin}(\text{Index}^2(16.i, 16.j)))$ ;
- 12     **end**
- 13 **end**
- 14 **Return** S-Box;
- 15 To calculate inverse S-Box
- 16 Calculate  $\text{inv}[F] \leftarrow \text{inverse of } [F]_{8 \times 8}$  over  $Z_2$ ;
- 17 **for**  $j=1$  to 16 **do**
- 18     **for**  $i=1$  to 16 **do**
- 19          $\text{inv}.(S\text{-Box})(i, j) = \text{Bin2Dec}(\text{mod}(\text{inv}.[F]_{8 \times 8} \times [\text{Dec2Bin}(\text{Index}^2(16.i, 16.j))]_{8 \times 1}, 2) \oplus \text{Dec2Bin}(SB(i, j)))$ ;
- 20     **end**
- 21 **end**
- 22 **Return** Inv.(S-Box);

---

illustration, we consider the parameter values as  $A = 15.02154872$ ,  $B = 3.50142547$ ,  $\beta = 5.02314723$ ,  $\alpha = 10.00148752$ ,  $IC_1 = 0.2501254781$ ,  $IC_2 = 0.2712548731$  so that  $a = g^7 + g^5 + g^3 + 1$  and  $b = g^7 + g^6 + g^3 + g^2$ . The extracted points  $P(x, y)$  on the elliptic curve  $E_{2^8}(a, b)$  are shown in Fig. 11. In what follows, we consider the

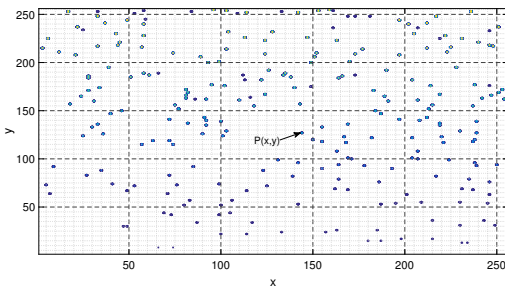


Fig. 11: Extracted points on the elliptic curve  $E_{2^8}(a, b)$  over the field  $GF_{2^8}$  are shown

control parameters and the initial conditions that give rise the hyperchaotic states of the enhanced Duffing map (3). The hyperchaotic sequences  $\{x\}$  and  $\{y\}$  so generated are then transformed over the Galois field

$GF_{2^8}$  into two new sequences as follows:

$$\begin{cases} x_1 = \text{floor}(\text{mod}(x \times 10^5, 256)), \\ y_1 = \text{floor}(\text{mod}(y \times 10^5, 256)). \end{cases}$$

The new sequences  $\{x\}$  and  $\{y\}$  along with the extracted points  $P(x, y)$  of the elliptic curve over the Galois field  $GF_{2^8}$ , the primitive polynomial  $f(x)$  and the field matrix  $F$  are then used to construct the S-box. The corresponding algorithm is given in Algorithm 3.

#### 4.3 Diffusion process

An image encryption algorithm has the ability to defeat chosen-plaintext attack when it has an efficient diffusion process. Therefore, this section introduces a new algorithm based on the field matrix  $F$ , S-Box, and the hyperchaotic sequence  $\{y\}$ . The process is described as follows:

Step 1 : The pixel values of  $S_{c_{m \times n}}$  are divided into  $S_{c_{k \times k}}^i$ , where  $k = 1, 2, \dots, 16$ , and  $i = 1, 2, \dots, \frac{m \times n}{K^2}$ .

Step 2 : Using the generated hyperchaotic sequence  $\{y\}$  by the enhanced map,  $Sy \leftarrow \text{ceil}(\text{mod}(y \times 10^5, 256))$  is calculated.

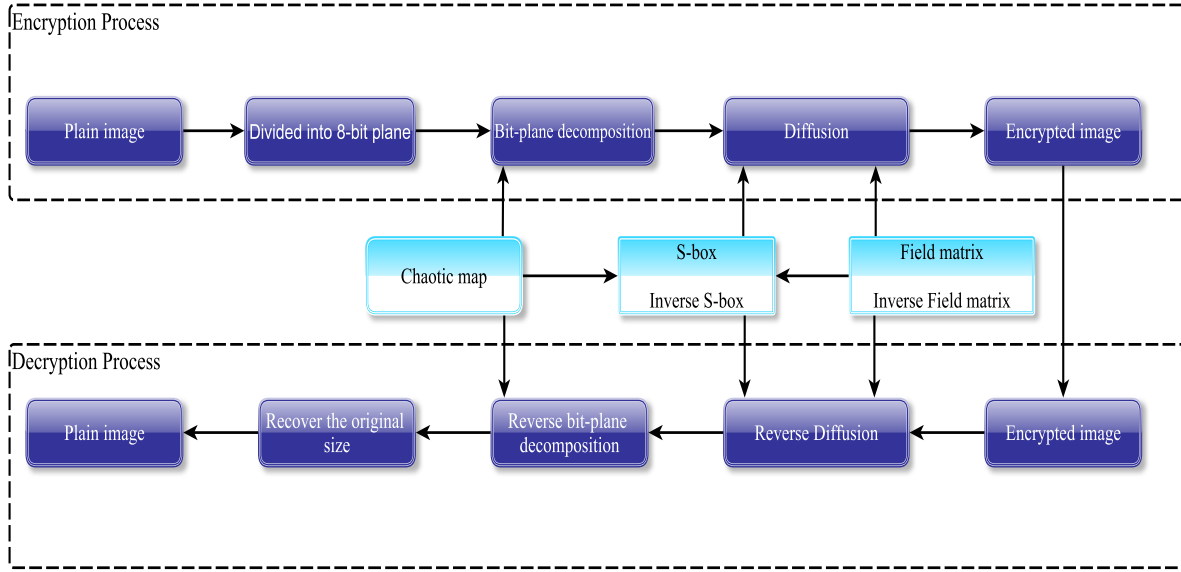


Fig. 12: Schematic diagram of the proposed image encryption and decryption algorithm.

Step 3 : The new scramble image matrix  $SC_{k \times k}^i$  is generated by the field matrix, which can be defined as  $SC_{k \times k}^i \leftarrow Bin2Dec(mod([F]_{8 \times 8} \times Dec2Bin(SC_{k \times k}^i, S_{(i_1, j_1, l)}), 256))$  where  $i_1, j_1 = 1, 2, \dots, k$  and  $l = 1, 2, \dots, i$ .

Step 4 : The block cipher image (CI)  $CI_{k \times k}^i$  is obtained by the bitwise XOR operation among  $SC_{k \times k}^i$ , S-Box and the sequence  $S_y$ .

Step 5 : The cipher image is obtained by reshaping  $CI_{k \times k}^i$  into  $CI_{m \times n}$  as:  $CI_{m \times n} \leftarrow reshape(CI_{k \times k}^i, m, n)$

for  $i_1, j_1 = 1, 2, \dots, k$  and  $l = 1, 2, \dots, i$  with  $k = 1, 2, \dots, 16$  and  $i = 1, 2, \dots, \frac{m \times n}{k^2}$ .

Step 6 : Calculate the scramble image matrix using the bitwise XOR operation as

$SC_{k \times k}^i(k1, k2, i2) \leftarrow mod((mod((inv.(S-Box(k1, k2)) \oplus CI_{k \times k}^i(k1, k2, i2)), 256) \oplus inv.Sy_{k \times k}^i(k1, k2, i2)), 256)$  for  $k_1, k_2 = 1, 2, \dots, k$  and  $i_2 = 1, 2, \dots, i$  with  $k = 1, 2, \dots, 16$  and  $i = 1, 2, \dots, \frac{m \times n}{k^2}$ .

Step 5 : Reshape the scramble image as  $SC_{m \times n} \leftarrow reshape(SC_{k \times k}^i, m, n)$ .

Step 6 : Descramble the scramble image using the same Algorithm 1 to recover the plain image.

#### 4.4 The process of decryption

The receiver section gets the cipher image along with the initial condition and control parameters of the enhanced map (3). Then the receiver constructs the field matrix  $F$  and the S-box, which are considered as secret key. Using the elliptic curve, hyperchaotic sequences, and the secret key, the receiver can construct the inverse field matrix and the inverse S-Box which represent the original key. Finally, the plain-image is recovered by the following decryption process.

Step 1 : The cipher image  $CI_{m \times n}$  is divided into  $CI_{k \times k}^i$  for  $k = 1, 2, \dots, 16$  and  $i = 1, 2, \dots, \frac{m \times n}{k^2}$ .

Step 2 : Having obtained the inverse field matrix ( $inv.(F)$ ), the chaos sequence  $\{y\}$  from the Duffing map and  $Sy \leftarrow ceil(mod(y \times 10^5, 256))$ , calculate  $inv.(Sy) \leftarrow inv.(F) \times Sy_{k \times k}^i$  for  $k = 1, 2, \dots, 16$  and  $i = 1, 2, \dots, \frac{m \times n}{k^2}$ , and construct the inverse S-Box using the algorithm 3.

Step 3 : Obtain the new cipher block matrix as  $CI_{k \times k}^i \leftarrow Bin2Dec(mod(inv.[F]_{8 \times 8} \times Dec2Bin(CI_{k \times k}^i, S_{(i_1, j_1, l)}), 256))$

## 5 Simulation results and key analysis

In this section, the proposed image encryption algorithm is simulated to demonstrate its efficiency. Moreover, the robustness of the employed key is investigated by performing the key space and the key sensitivity analyses.

### 5.1 Encrypting different kinds of images

To illustrate the ability of the proposed image encryption algorithm for ciphering different types of images, Figure 13 depicts the encryption results with uniformly distributed histograms of various kinds of plain-images including Grey scale, RGB, Sketch, and Hand writing images with the size of  $(512 \times 512)$ . Moreover, this figure shows the encryption of a medical image of size

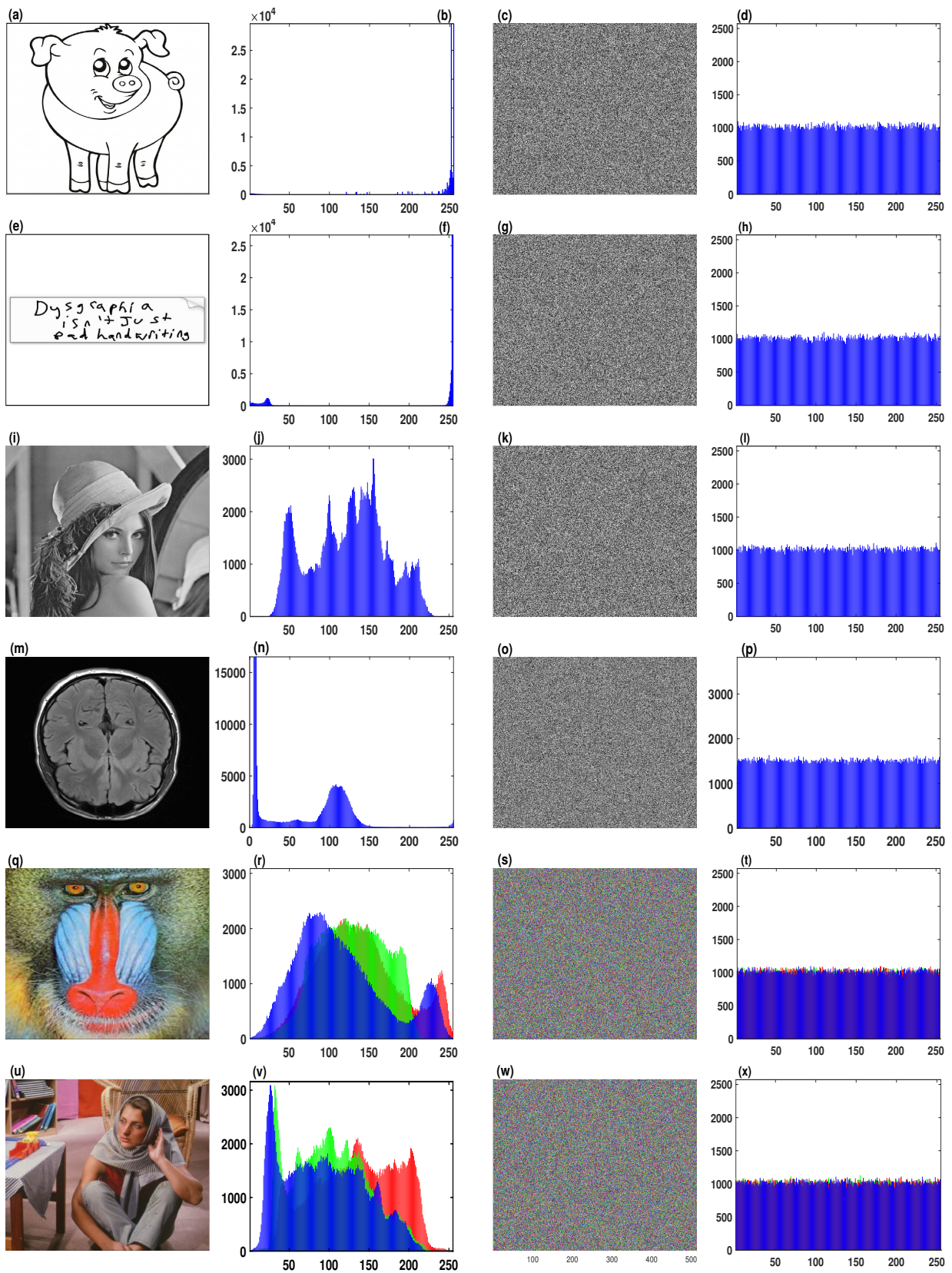


Fig. 13: Encryption results of different images: the first column depicts the plain-images including animal sketch image, hand writing image, Lena grey-scale image, medical image, animal color image, Barbara color image; the second column depicts histograms of the plain-images; the third column depicts the encryption of the plain-images; the fourth column depicts histograms of the encrypted images.

(630 × 630) with its histogram. It can be seen from these results that the proposed encryption algorithm can effectively encrypt various kinds of images.

## 5.2 Key space analysis

Typically, the security key of chaos-based cryptography contains two main components, namely the initial conditions and the control parameters of the employed chaotic map. In the proposed encryption algorithm, the parameters and the initial conditions of the enhanced Duffing map (3) are the main roots of the secret keys. Each parameter and initial values are considered with 15 to 16 decimal places, which means that the complexity of each parameter and the initial value is  $2^{52}$ . Besides that, the hyperchaotic sequences of the enhanced map (3) are generated by the parameters and the initial conditions for constructing the field matrix and the S-box. So, the key space in producing  $F$  and the S-Box is  $2^{64}$  (for 64-bit operation) ×  $2^{102}$  (initial conditions) =  $2^{166}$ , and the total key combinations is  $2^{478}$  i.e., the size of the key in the proposed algorithm is 478 bits. Consequently, the security key of the proposed algorithm achieves the standard requirement [21].

Furthermore, the total time to break an encrypted image is calculated as follows

$$Y = \frac{T \times 1000}{FLOPS} \times 3153600,$$

where  $Y$  is the total years to break an encrypted image, and  $T$  is the total security key space. A super computer has  $10^{15}$  floating-point operation per second (FLOPS). So, the total time to break the encrypted image by the proposed algorithm is approximately  $1.230593278 \times 10^{137}$  years.

## 6 Security analysis

The most important indicator to evaluate an image encryption algorithm is the security performance of its encrypted image. This section introduces an analysis framework to investigate the security of the encrypted images by the proposed algorithm.

### 6.1 Robustness analysis of noise and data loss

Different kinds of noise and data loss can corrupt the encrypted images. So, the image encryption algorithms should be able to resist these kinds of noise and data loss. The first and second columns of Figure 14 demonstrate the quality results of the recovered image when

the corresponding encrypted image undergoes Gaussian noise with 5% density, as well as salt and pepper noise with 12% density. It can be observed that although the encrypted images have noise, the corresponding recovered images contain the most visual information of the original images. Besides that, the proposed algorithm has successfully recovered the images with Peak Signal-to-Noise Ratio (PSNR) equal to 22.32 and Mean Square Error (MSE) equal to 381.08 even with an addition of 5% Gaussian noise. Meanwhile, the obtained PSNR and MSE for addition of 12% of salt and pepper noises are 17.3648 and 1192 respectively. Moreover, the third column of Figure 14 shows that the recovered images by the proposed algorithm can still be recognizable when the encrypted image has 15% data loss. As a result, the proposed encryption algorithm can resist different kinds of noise and data loss.

### 6.2 Differential attack resistance

A vulnerable encryption scheme could be attacked by observing the change in the encrypted images when a small change or modification happens in the corresponding plain image. This type of attack is namely chosen plaintext attack or differential attack. The NPCR and UACI tests could be employed to estimate the resistance of encryption algorithms against differential attacks. The NPCR indicates the pixel change rate, while the UACI indicates the unified averaged changed intensity. These two measures are as follows:

$$NPCR = \frac{\sum_{i,j}^{m,n} D(i,j)}{m \times n} \times 100, \quad (7)$$

where  $D(i,j)$  is the change of the pixel values from the plain-image to the encrypted image due to the encryption process, in which

$$D(i,j) = \begin{cases} 0 & \text{when } P(i,j) = CI(i,j) \\ 1 & \text{when } P(i,j) \neq CI(i,j). \end{cases} \quad (8)$$

As the pixel values are changed, the UACI can be used to determine the average intensity of the difference between the original and the encrypted image, where

$$UACI = \frac{1}{m \times n} \sum_{i,j}^{m,n} \frac{|P(i,j) - CI(i,j)|}{255} \times 100. \quad (9)$$

However, Wu [34] presented a new standard of NPCR and UACI measures for better estimating the ability of an encryption algorithm for resisting differential attack. In this regard, an image encryption algorithm can pass



Fig. 14: Robustness analysis of noise and data loss: (a) and (d) depict the encrypted image with 5% Gaussian noise, and the decrypted image respectively; (b) and (e) depict the encrypted image with 12% salt and pepper noise, and the corresponding decrypted image respectively; (c) and (f) depict the encrypted image with 15% data loss, and the decrypted image respectively.

the NPCR test when its NPCR value is bigger than a level  $\alpha$ , which is given by the following equations.

$$\begin{aligned} N_{\alpha}^* &= \mu_N - \Phi^{-1}(\alpha) \sqrt{\frac{F}{255}}, \\ N_{\alpha}^* &= \frac{F - \Phi^{-1}(\alpha) \sqrt{\frac{F}{255}}}{F + 1}, \end{aligned} \quad (10)$$

where  $\Phi^{-1}$  is the inverse CDF of the standard Normal distribution  $N(0, 1)$ , and  $F$  is the largest supported pixel value compatible with the cipher text image format. An encryption algorithm successfully passes the UACI test when the simulation value is in the range of  $UACI \in (U_{\alpha}^-, U_{\alpha}^+)$ . Here,  $U_{\alpha}^-$  and  $U_{\alpha}^+$  are given by

$$\begin{aligned} U_{\alpha}^- &= \mu_U - \Phi^{-1}(\alpha/2) \sigma_U, \\ U_{\alpha}^+ &= \mu_U + \Phi^{-1}(\alpha/2) \sigma_U, \end{aligned} \quad (11)$$

with

$$\begin{aligned} \sigma_U &= \sqrt{\frac{(F+2)(F^2+2F+3)}{18(F+1)^2 \times 255F}}, \\ \mu_U &= \frac{F+2}{3F+3}. \end{aligned} \quad (12)$$

In this test, for each plaint image, namely,  $PI_1$ , we generate an another image, namely,  $PI_2$  by selecting a pixel from  $PI_1$  and changing its value by 1-bit. Subsequently, the UPCR and UACI values can be calculated by generating the encrypted images of both  $PI_1$  and  $PI_2$ . The NPCR and UACI results of 27 different types of images, which are taken from USC-SIPI Miscellaneous data set and which have been encrypted by the proposed algorithm and several other schemes, are illustrated in Table 3. From these results it is found that that the proposed algorithm has superior or competitive performance in defending the differential attack.

Table 3: The NPCR and UACI values are calculated with  $\alpha = 0.05$  for different images using some existing schemes and our scheme.

Index	Image size	Our scheme	LICM[17]	ICMIE[18]	Zhou[14]	Wu[13]	Liao[12]
NPCR	$256 \times 256 \geq 99.5693\%$	6/6	6/6	6/6	6/6	6/6	0/6
	$512 \times 512 \geq 99.5893\%$	18/18	17/18	18/18	17/18	17/18	1/18
	$1024 \times 1024 \geq 99.5994\%$	3/3	3/3	3/3	3/3	2/3	0/3
Pass Rate		27/27	26/27	27/27	26/27	25/27	1/27
UACI	$256 \times 256 (33.2824 - 33.6447)$	6/6	6/6	6/6	1/6	6/6	0/6
	$512 \times 512 (33.3730 - 33.5541)$	18/18	16/18	18/18	4/18	15/18	0/3
	$1024 \times 1024 (33.4183 - 33.5088)$	3/3	2/3	3/3	2/3	1/3	0/3
Pass Rate		27/27	24/27	27/27	7/27	22/27	0/27

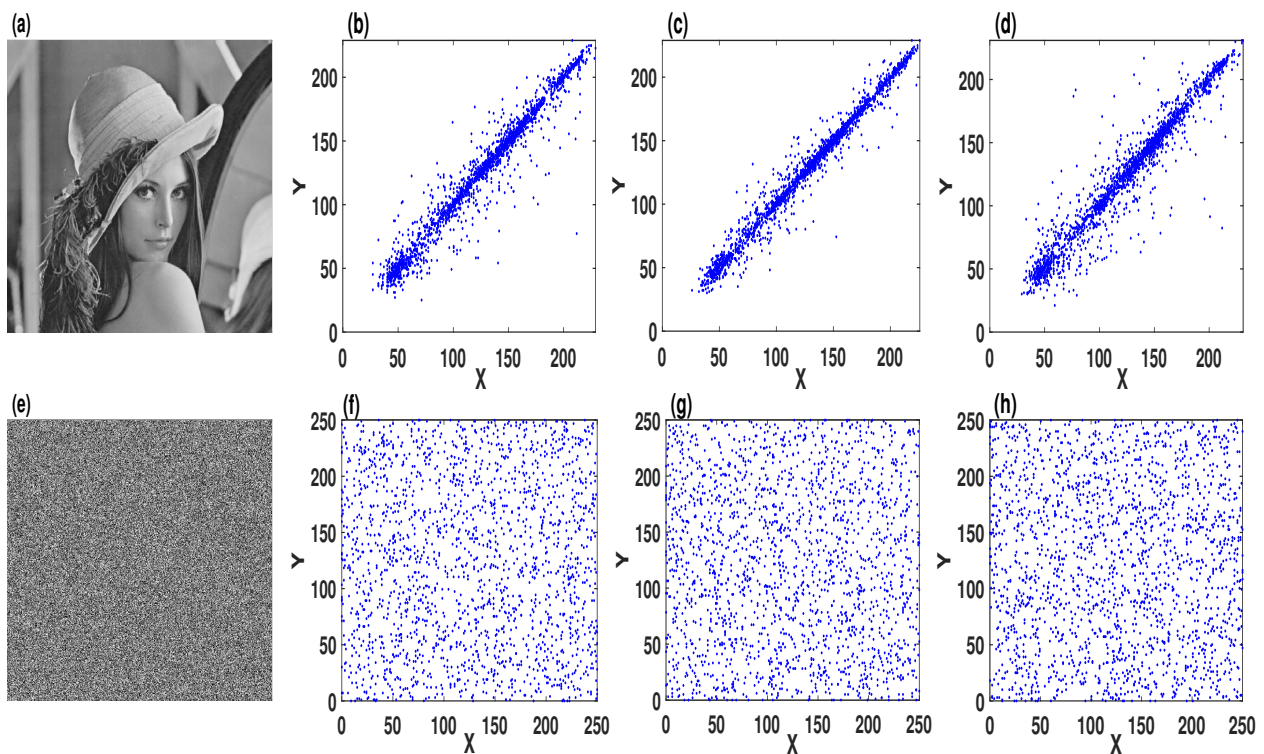


Fig. 15: The correlation of the neighboring pixel pairs: the first column depicts the plain-image and the corresponding encrypted image; the second column depicts the horizontal direction of plain-image and the encrypted image; the third column depicts the vertical direction of the plain-image and the encrypted image; the fourth column depicts the diagonal direction of the plain-image and the encrypted image.

### 6.3 Resisting Noise Attack Analysis

The encoded image version is inevitably exposed to different types of noises, when the data passes through a real communication channel. This noise can cause problems during the acquisition of the original image. Therefore, the algorithm should be noise resistant, so that the encryption scheme can be valid. The Peak Signal-to-Noise Ratio (PSNR) is used to measure the quality

of the decoded image after the attacks. For the image components, PSNR can be obtained by the following formulation

$$PSNR = 10 \times \log_{10} \left( \frac{255 \times 255}{MSE} \right) \text{ DB} \quad (13)$$

where

$$MSE = \frac{1}{m \times n} \sum_{i=1}^m \sum_{j=1}^n \| (i, j) - DCI(i, j) \| \quad (14)$$

MSE is the mean square error between the original and recovered images and is represented as P and DCI respectively, with the size of  $m \times n$ . The first and second columns of Fig. 14 demonstrate the quality results of the recovered image when the corresponding encrypted image undergoes Gaussian noise with 5% density, as well as salt and pepper noise with 12% density. The MSE and PSNR of these decoded images are shown in Table 4. From this table and Fig. 14, we can understand that the original image is entirely obtained again, which is noticeable, the PSNR value is near about  $30dB$  when Gaussian noise density 1%,  $22dB$  with 5% density and  $18dB$  for 12% density and the decoded images are highly correlated with original image.

#### 6.4 Key sensitivity analysis

The employed key of an image encryption scheme is considered as highly sensitive when the encrypted image cannot be recovered due to a slight difference in one of the key components. To visualize the key sensitivity of the proposed encryption algorithm, we set the main root of the secrete keys, which represent the initial conditions and parameters of the map (3), as  $A = 15.02154872$ ,  $B = 3.50142547$ ,  $\beta = 5.02314723$ ,  $\alpha = 10.00148752$ ,  $IC_1 = 0.2501254781$ ,  $IC_2 = 0.2712548731$ . Subsequently, we change  $14^{th}$  decimal places in the parameters, or initial conditions, or both to obtain three other keys. Figure 16 demonstrates the key sensitivity in the decryption process with the original key and the modified keys. We consider different image sizes and calculate the NPCR and UACI values corresponding to the encryption with the actual parameters and initial condition as well as the decryption with wrong parameters and initial condition. The results are given in Table 5. Thus, from Table 5 it is clear that even with a small change, i.e., a change in the 14-th decimal place of the parameters or initial condition, the change in the pixel values is more than 99% after decryption with wrong initial condition and/or parameters.

#### 6.5 Correlation analysis

The adjacent pixels of the original image are highly correlated along the vertical, diagonal, and horizontal directions. Thus, an efficient encryption algorithm can resist a statistical attack when the adjacent pixels of its encrypted image is nearly zero. To calculate the pixels correlation, let us first define the covariance between a pair of pixel values  $x$  and  $y$ , which is given by

$$Cov(x, y) = E[(x - E(x))(y - E(y))], \quad (15)$$

where  $E(x)$  and  $E(y)$  are the means. Now, the correlation coefficients can be calculated by

$$\rho_{xy} = \frac{Cov(x, y)}{\sigma(x)\sigma(y)}, \quad \sigma(x), \sigma(y) \neq 0, \quad (16)$$

where  $\sigma(x)$  and  $\sigma(y)$  are the standard deviations of the distribution of the pixel.

In our analysis, adjacent pixels in horizontal, vertical, and diagonal directions are randomly chosen from both plain and encrypted images, as shown in 15. As can be seen, most of the pixels are close to the diagonal line of axis for the plain image. Meanwhile, the pixels of the encrypted image distribute randomly on the whole space. Furthermore, quantitative and comparison results of adjacent pixels correlations of Lena image, which is encrypted by the proposed encryption algorithm and other existing schemes, are illustrated in Table 6. Clearly, the  $\rho_{xy}$  values of our scheme are more closer to 0, and superior and competitive than those of some other schemes.

#### 6.6 Local Shannon Entropy

The Local Shannon entropy, which quantitatively measures the distribution of information, is used to estimate the randomness of an encrypted image. Mathematically, it is defined as

$$\overline{H_{k, T_B}} = \sum_{i=1}^k \frac{H(s_i)}{k} \quad (17)$$

where  $s_1, s_2, \dots, s_k$  are  $k$  selected blocks with  $T_B$  pixels of a chosen image. If  $\overline{H_{k, T_B}}$  is in the interval of  $(h_{left}, h_{right})$ , then the cipher text image will be considered as passing the test. Next, we calculate the critical values  $h_{left}$  and  $h_{right}$  with  $\alpha$  level of significance in a  $Z$ -test as follows:

$$\begin{aligned} h_{left} &= \mu_{\overline{H_{k, T_B}}} - \Phi_{\alpha/2}^{-1} \sigma_{\overline{H_{k, T_B}}} \\ h_{right} &= \mu_{\overline{H_{k, T_B}}} + \Phi_{\alpha/2}^{-1} \sigma_{\overline{H_{k, T_B}}} \end{aligned} \quad (18)$$

where  $\Phi^{-1}$  is the inverse cumulative density function of the standard normal distribution  $N(0, 1)$  and  $\mu_{\overline{H_{k, T_B}}}$ , and  $\sigma_{\overline{H_{k, T_B}}}$  be the mean and variance of Local Shannon entropy calculated in  $k$  non overlapping blocks.

In this test, we select 27 different images from USC-SIPI Miscellaneous data set, and then encrypt these images by various image encryption algorithms. According to the recommendation in [37], we set the parameters  $(k, T_B) = (30, 1936)$  and  $\alpha = 0.001$ , then an image is considered to pass the test if the obtained Local Shannon Entropy falls into the interval  $(7.901515698, 7.903422936)$ . Table 7 lists Local Shannon entropy results of the encrypted image. The results demonstrate that the proposed algorithm successfully pass the test.

Table 4: MSE and PSNR analysis of plain image and decrypted image in which cipher image is introduced with Gaussian Noise with different level of density 1%, 5% and 12%.

Image	Noise Density	MSE			PSNR(dB)		
		R	G	B	R	G	B
Barbara	0.01	105.2502	111.2145	108.23	28.8560	28.1520	27.9289
	0.05	381.0801	378.5205	382.8906	22.3578	22.1245	22.1345
	0.12	1192.2452	1188.3542	1194.2578	17.3648	17.2548	17.2045
Lena	0.01	102.5625	103.2541	104.3252	29.7824	30.2569	29.1245
	0.05	370.2356	369.8567	372.5687	23.5689	23.5478	23.7482
	0.12	1178.2586	1174.6583	1180.8563	18.3562	18.6524	18.5242
Animal	0.01	104.1625	105.5141	106.2152	29.1824	29.1269	29.1451
	0.05	375.1256	374.1057	377.1067	22.1068	22.1054	22.4082
	0.12	1198.2045	1201.3212	1199.1057	16.4648	16.2554	16.3445

Table 5: The encrypted and decrypted NPCR and UACI values for different image sizes are shown due to a small change in the parameters and/or initial condition.

Index	Image size	Encrypted using actual initial conditions	Decrypted using wrong initial conditions
NPCR	$256 \times 256 \geq 99.5693\%$	99.655151367%	99.588012695%
	$512 \times 512 \geq 99.5893\%$	99.633407592%	99.623489379%
	$1024 \times 1024 \geq 99.5994\%$	99.612331390%	99.608325958%
UACI	$256 \times 256 (33.2824 - 33.6447)$	33.353662490%	33.47766058%
	$512 \times 512 (33.3730 - 33.5541)$	33.492037854%	33.485890501%
	$1024 \times 1024 (33.4183 - 33.5088)$	33.500159085%	33.501732840%

Table 6: The correlation coefficients of the plain-image and the encrypted image by various methods.

Index	Lena image	Our scheme	LICM[17]	ICMIE[18]	2D-LCCM[5]	Xu[15]	Liao[12]
Horizontal	0.971921627	-0.0009	0.0019	-0.0008	-0.0009	0.0230	0.0127
Vertical	0.9865777	0.0015	0.0012	-0.0013	-0.0005	0.0019	-0.0190
Diagonal	0.96064343	-0.0010	0.0009	0.0018	0.0029	0.0034	-0.0012

### 6.7 Randomness test for S-box and encrypted image

To test the randomness of the proposed S-box and the encrypted image, we use statistical tests package, namely, NIST-800-22. This package has several tests, and each test provides a p-value, which can discover the non-random regions from several sides. If the p-value  $\geq 0.01$ , then the truncated sequence passes the test. Table 8 lists NIST-800-22 results for the S-box and encrypted image. They successfully pass all the tests. That means the S-box and the pixel value of the encrypted image are random.

### 6.8 Computational and time complexity analyses

In the row-column permutation or the confusion stage, the computational complexities to perform the row shuffling and the column shuffling operations using the chaotic

sequence, respectively, are  $\mathbf{O}(m)$  and  $\mathbf{O}(n)$ , where  $m$  and  $n$  are the pixel values. So, the computational complexity to perform the pixel shuffling is  $8(m + 8n)$ .

In the diffusion stage, the images are first divided into scramble matrices  $SC_{k \times k}^i$  for  $k = 1, 2, \dots, 16$  and  $i = 1, 2, \dots, \frac{m \times n}{k^2}$ . This means that each block is of the order of  $k \times k$  in which each vector is multiplied by the field matrix of order  $8 \times 8$ . Thus, the time complexity is given as  $\mathbf{O}(\frac{64 \times m \times n}{k^2})$ . Also, in the final encryption in which bitwise-XOR is performed, the time complexity is given as  $72(m + n)$ . So, the total time complexity is  $\frac{64 \times m \times n}{k^2} + 8(10m + 17n)$ . As an illustration, we consider a Barbara image of size  $512 \times 512$ , encrypt it 60 times using R2016a Matlab software with i3-4005 CPU 1.7 GHz, 4-Gb RAM, finally compare with different existing schemes to show the efficiency of our proposed algorithm. The results are displayed in Table 9.

Table 7: The local Shannon entropy analysis with  $\alpha = 0.001$   $k = 30$ ,  $T_B = 1936$  of images which are collected from USC-SIPI Miscellaneous data-set

Image name	Our scheme	Wu [13]	Wang[14]	Liao [12]	Shen[19]	Kumar[20]
5.1.09	7.902212	7.901985	7.899212	7.904191	7.997181	7.999602
5.1.10	7.901902	7.902731	7.901125	7.902371	7.997282	7.999626
5.1.11	7.902425	7.902446	7.901521	7.900799	7.997235	7.90233
5.1.12	7.902481	7.902556	7.899145	7.903374	7.902974	7.999652
5.1.13	7.902075	7.902688	7.900901	7.904566	7.901951	7.999612
5.1.14	7.902918	7.903474	7.900112	7.903111	7.902577	7.901996
5.2.08	7.903094	7.903953	7.902325	7.901762	7.903408	7.999608
5.2.09	7.902541	7.902233	7.902001	7.905854	7.997842	7.902996
5.2.10	7.902029	7.900714	7.902721	7.902768	7.997485	7.999699
5.3.01	7.902361	7.902727	7.902432	7.901040	7.996482	7.999658
5.3.02	7.903230	7.903182	7.902631	7.900981	7.903331	7.90421
7.1.01	7.901931	7.902173	7.902002	7.902145	7.992482	7.999615
7.1.02	7.902419	7.900879	7.902821	7.902157	7.997842	7.999678
7.1.03	7.902170	7.902543	7.902325	7.900645	7.991748	7.901996
7.1.04	7.903219	7.901126	7.902411	7.904141	7.992748	7.902539
7.1.05	7.902091	7.903579	7.902251	7.900027	7.996748	7.902605
7.1.06	7.902850	7.901930	7.902762	7.901736	7.902012	7.902311
7.1.07	7.902258	7.903000	7.902575	7.900802	7.997485	7.902568
7.1.08	7.902022	7.903197	7.902114	7.900944	7.902748	7.902512
7.1.09	7.902255	7.902308	7.902709	7.905658	7.997485	7.901951
7.1.10	7.902032	7.899542	7.902525	7.893848	7.991748	7.903225
7.2.01	7.902038	7.902772	7.902224	7.904525	7.995748	7.999652
Boat.512	7.901863	7.901908	7.902616	7.900712	7.992748	7.999656
Gray21.512	7.902807	7.900170	7.902020	7.902149	7.993748	7.999655
House	7.90228701	7.903580	7.904501	7.902156	7.998748	7.999665
Ruler.512	7.901977	7.903265	7.902454	7.901428	7.996748	7.999678
Numbers.512	7.903047	7.903615	7.902535	7.903579	7.997748	7.999675
Mean	7.902391	7.902381	7.903141	7.902128	7.992748	7.999675
Pass Rate	27/27	17/27	22/27	10/27	7/27	11/27

$h_{left} = 7.901515698$   
 $h_{right} = 7.903422936$

Table 8: Randomness test of s-box and Encrypted image

Test name	P-value(for randomness $\geq 0.01$ )		Result
	S-box	Encrypted Image	
Block frequency test	0.2442	0.4071	Pass
The Runs Test,	0.7493	0.6758	Pass
The Longest-Run-of-Ones	0.2465	0.4465	Pass
The Binary Matrix Rank Test,	0.4312	0.4312	Pass
The Discrete Fourier Transform	0.0621	0.6555	Pass
The Cumulative Sums	0.5283	0.6170	Pass
The Approximate Entropy Test	0.6825	0.6892	Pass
The Non-overlapping Template	0.7784	0.7204	Pass
The Overlapping Template	0.4432	0.5592	Pass
The Linear Complexity Test	0.5517	0.5175	Pass
The Serial Test	P-value1=0.9070; P-value2=0.8547 P-value1=0.8879; P-value2=0.8041		Pass

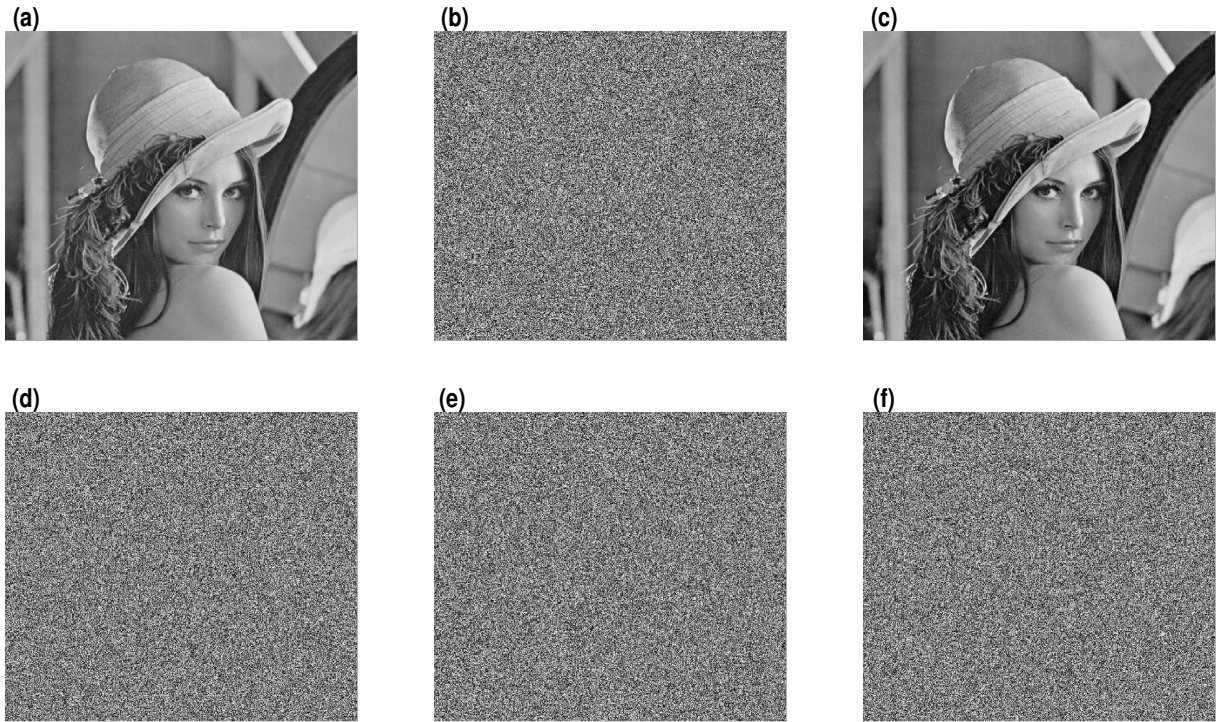


Fig. 16: Key sensitivity analysis: (a) plain-image, (b) the encrypted image, (c) the decrypted image with the right key. Subplots (d)-(f) are the decrypted images with wrong keys. They are obtained due to a slight change in both the parameters and the initial conditions [subplot (d)], in the parameters only [subplot (e)], in the initial condition only [subplot (f)].

Table 9: The computational complexity and the time complexity using different algorithms

Algorithm	Computational complexity	Execution time
LICM [17]	$m \log(8n) + 8n \log(m) + 2(m + 8n)$	1.2395278
ICMIE [18]	$2(m \log(n) + mn)$	1.1858623
2D-LCCCM[5]	$(5 + CR) \times m \times n$	1.1256258
Cross-coupled chaos [38]	$2 \max(m, n) + 9(m + n)$	1.1217369
Mixed image element and chaos [39]	$\frac{(m \log(n) + n \log(m))mn}{64}$	2.1235896
Our Scheme	$\frac{64 \times m \times n}{k} + 8(10m + 17n)$	1.1019249

## 7 Conclusion

A low-dimensional discrete chaotic system such as the Duffing map can exhibit complicated multistability behaviors. The coexistence of chaotic attractors with periodic orbits as well as the coexistence of two chaotic attractors in the 2D Duffing map are shown. We have introduced the Sine-Cosine chaotification technique to enhance chaos complexity in the multistable regions of the 2D Duffing map. The proposed chaotification technique can be easily generalized to other low-dimensional chaotic maps. Several performance evaluations includ-

ing the trajectory, Lyapunov exponents, bifurcations, FIPS 140-2 test, and Sample entropy have demonstrated that the enhanced Duffing map exhibits a wide hyperchaotic range, high randomness and extreme unpredictability. Furthermore, its hyperchaotic sequences appear in a large area in the 2D phase space without exhibiting periodic behaviors. Consequently, the enhanced Duffing map could be a better choice than other existing chaotic maps for cryptography applications. Thus, we propose an image encryption algorithm, which achieves the confusion and diffusion processes by

hyperchaotic sequences, elliptic curve, and S-box. Simulation results have revealed that the proposed encryption algorithm can give the users a flexibility to encrypt several kinds of images such as Grey scale, Medical, and RGB images with a higher level of security. As the proposed image encryption algorithm based on the enhanced Duffing map has high security and efficiency, our future work will investigate its application in video encryption.

### Compliance with ethical standards

**Conflict of interest** All authors declare that they have no conflict of interest.

**Ethical approval** This article does not contain any studies with human participants or animals performed by any of the authors.

**Informed Consent** Not applicable.

**Author Contributions** Hayder Natiq conceived and designed the analysis, collected the data, performed the analysis, wrote the paper; Animesh Roy conceived and designed the analysis, wrote the paper; conceptualization and supervision, Santo Banerjee; methodology, A. P. Misra; software, N. A. A. Fataf.

### References

1. Cao, Chun, Kehui Sun, and Wenhao Liu. "A novel bit-level image encryption algorithm based on 2D-LICM hyperchaotic map." *Signal Processing* 143 (2018): 122-133.
2. Wu, X., Wang, D., Kurths, J., & Kan, H. "A novel lossless color image encryption scheme using 2D DWT and 6D hyperchaotic system." *Information Sciences* 349 (2016): 137-153.
3. Chai, Xiuli, Yiran Chen, and Lucie Broyde. "A novel chaos-based image encryption algorithm using DNA sequence operations." *Optics and Lasers in engineering* 88 (2017): 197-213.
4. Zhang, Y., Zhang, L. Y., Zhou, J., Liu, L., Chen, F., & He, X. "A review of compressive sensing in information security field." *IEEE access* 4 (2016): 2507-2519.
5. Nan, S. X., Feng, X. F., Wu, Y. F., & Zhang, H. "Remote sensing image compression and encryption based on block compressive sensing and 2D-LCCCM." *Nonlinear Dynamics* 108.3 (2022): 2705-2729.
6. Luo, Yuling, Minghui Du, and Junxiu Liu. "A symmetrical image encryption scheme in wavelet and time domain." *Communications in Nonlinear Science and Numerical Simulation* 20.2 (2015): 447-460.
7. Natiq, H., Al-Saidi, N. M., Obaiys, S. J., Mahdi, M. N., & Farhan, A. K. "Image Encryption Based on Local Fractional Derivative Complex Logistic Map." *Symmetry* 14.9 (2022): 1874.
8. Ibrahim, R. W., Natiq, H., Alkhayyat, A., Farhan, A. K., Al-Saidi, N. M., & Baleanu, D. "Image encryption algorithm based on new fractional beta chaotic maps." *CMES-COMPUTER MODELING IN ENGINEERING & SCIENCES* 132.1 (2022): 119-131.
9. Natiq, H., Banerjee, S., Misra, A. P., & Said, M. R. M. "Degenerating the butterfly attractor in a plasma perturbation model using nonlinear controllers." *Chaos, Solitons & Fractals* 122 (2019): 58-68.
10. Natiq, H., Kamel Ariffin, M. R., Asbullah, M. A., Mahad, Z., & Najah, M. "Enhancing chaos complexity of a plasma model through power input with desirable random features." *Entropy* 23.1 (2020): 48.
11. Al-Saidi, N. M., Younus, D., Natiq, H., Ariffin, M. R. K., Asbullah, M. A., & Mahad, Z. "A new hyperchaotic map for a secure communication scheme with an experimental realization." *Symmetry* 12.11 (2020): 1881.
12. Liao, Xiaofeng, Shiyue Lai, and Qing Zhou. "A novel image encryption algorithm based on self-adaptive wave transmission." *Signal processing* 90.9 (2010): 2714-2722.
13. Wu, Y., Noonan, J. P., Yang, G., & Jin, H. "Image encryption using the two-dimensional logistic chaotic map." *Journal of Electronic Imaging* 21.1 (2012): 013014.
14. Zhou, Yicong, Long Bao, and CL Philip Chen. "Image encryption using a new parametric switching chaotic system." *Signal processing* 93.11 (2013): 3039-3052.
15. Xu, L., Li, Z., Li, J., & Hua, W. "A novel bit-level image encryption algorithm based on chaotic maps." *Optics and Lasers in Engineering* 78 (2016): 17-25.
16. Hua, Zhongyun, and Yicong Zhou. "Image encryption using 2D Logistic-adjusted-Sine map." *Information Sciences* 339 (2016): 237-253.
17. Cao, Chun, Kehui Sun, and Wenhao Liu. "A novel bit-level image encryption algorithm based on 2D-LICM hyperchaotic map." *Signal Processing* 143 (2018): 122-133.
18. Cao, Weijia, Yujun Mao, and Yicong Zhou. "Designing a 2D infinite collapse map for image encryption." *Signal Processing* 171 (2020): 107457.

19. Shen, Honglian, et al. "A new chaotic image encryption algorithm based on transversals in a Latin square." *Entropy* 24.11 (2022): 1574.
20. Kumar, C. Madan, R. Vidhya, and M. Brindha. "An efficient chaos based image encryption algorithm using enhanced thorp shuffle and chaotic convolution function." *Applied Intelligence* 52.3 (2022): 2556-2585.
21. Alvarez, Gonzalo, and Shujun Li. "Some basic cryptographic requirements for chaos-based cryptosystems." *International journal of bifurcation and chaos* 16.08 (2006): 2129-2151.
22. Hua, Zhongyun, Binghang Zhou, and Yicong Zhou. "Sine-transform-based chaotic system with FPGA implementation." *IEEE Transactions on Industrial Electronics* 65.3 (2017): 2557-2566.
23. Hua, Zhongyun, and Yicong Zhou. "Image encryption using 2D Logistic-adjusted-Sine map." *Information Sciences* 339 (2016): 237-253.
24. Natiq, H., Al-Saidi, N. M. G., Said, M. R. M., & Kilicman, A. "A new hyperchaotic map and its application for image encryption." *The European Physical Journal Plus* 133.1 (2018): 1-14.
25. Hua, Z., Zhou, Y., Pun, C. M., & Chen, C. P. "2D Sine Logistic modulation map for image encryption." *Information Sciences* 297 (2015): 80-94.
26. Hua, Zhongyun, Yicong Zhou, and Hejiao Huang. "Cosine-transform-based chaotic system for image encryption." *Information Sciences* 480 (2019): 403-419.
27. Natiq, H., Said, M. R. M., Ariffin, M. R. K., He, S., Rondoni, L., & Banerjee, S. "Self-excited and hidden attractors in a novel chaotic system with complicated multistability." *The European Physical Journal Plus* 133.12 (2018): 1-12.
28. Rahim, M. A., Natiq, H., Fataf, N. A. A., & Banerjee, S. "Dynamics of a new hyperchaotic system and multistability." *The European Physical Journal Plus* 134.10 (2019): 1-9.
29. Natiq, H., Banerjee, S., Ariffin, M. R. K., & Said, M. R. M. "Can hyperchaotic maps with high complexity produce multistability?." *Chaos: An Interdisciplinary Journal of Nonlinear Science* 29.1 (2019): 011103.
30. Ding, Tongren, and Fabio Zanolin. "Time-maps for the solvability of periodically perturbed nonlinear Duffing equations." *Nonlinear Analysis: Theory, Methods & Applications* 17.7 (1991): 635-653.
31. Liu, Wenhao, Kehui Sun, and Congxu Zhu. "A fast image encryption algorithm based on chaotic map." *Optics and Lasers in Engineering* 84 (2016): 26-36.
32. Gao, Yinghui, and Bing Liu. "Study on the dynamical behaviors of a two-dimensional discrete system." *Nonlinear Analysis: Theory, Methods & Applications* 70.12 (2009): 4209-4216.
33. Richman, Joshua S., and J. Randall Moorman. "Physiological time-series analysis using approximate entropy and sample entropy." *American Journal of Physiology-Heart and Circulatory Physiology* (2000).
34. Wu, Yue, Joseph P. Noonan, and Sos Agaian. "NPCR and UACI randomness tests for image encryption." *Cyber journals: multidisciplinary journals in science and technology, Journal of Selected Areas in Telecommunications (JSAT)* 1.2 (2011): 31-38.
35. Patro, K. A. K., Soni, A., Netam, P. K., & Acharya, B. "Multiple grayscale image encryption using cross-coupled chaotic maps." *Journal of Information Security and Applications* 52 (2020): 102470.
36. Zhang, Xiaoqiang, and Xuesong Wang. "Multiple-image encryption algorithm based on mixed image element and chaos." *Computers & Electrical Engineering* 62 (2017): 401-413.
37. Y. Wu, Y. Zhou, G. Saveriades, S. Agaian, J.P. Noonan, P. Natarajan, Local Shannon entropy measure with statistical tests for image randomness, *Inf. Sci.* 222 (2013) 323–342.
38. Patro, K. A. K., Soni, A., Netam, P. K., & Acharya, B. "Multiple grayscale image encryption using cross-coupled chaotic maps." *Journal of Information Security and Applications* 52 (2020): 102470.
39. Zhang, Xiaoqiang, and Xuesong Wang. "Multiple-image encryption algorithm based on mixed image element and chaos." *Computers & Electrical Engineering* 62 (2017): 401-413.